

Structural and Electrical Properties of MoTe₂ and MoSe₂ Grown by Molecular Beam Epitaxy

Anupam Roy^{1*}, Hema C. P. Movva^{1*}, Biswarup Satpati², Kyoungwan Kim¹, Rik Dey¹, Amritesh Rai¹, Tanmoy Pramanik¹, Samaresh Guhahait^{1#}, Emanuel Tutuc¹ and Sanjay K. Banerjee¹

¹Microelectronics Research Center, The University of Texas at Austin, Austin, Texas 78758, USA

²Surface Physics and Material Science Division, Saha Institute of Nuclear Physics, 1/AF, Bidhannagar, Kolkata 700 064, India

*Address correspondence to anupam@austin.utexas.edu; hemacp@utexas.edu

#Presently at: Department of Physics, University of Maryland, College Park, MD 20742, USA

ABSTRACT: We demonstrate the growth of thin films of molybdenum ditelluride and molybdenum diselenide on sapphire substrates by molecular beam epitaxy. *In situ* structural and chemical analyses reveal stoichiometric layered film growth with atomically smooth surface morphologies. Film growth along the (001) direction is confirmed by X-ray diffraction, and the crystalline nature of growth in the 2H phase is evident from Raman spectroscopy. Transmission electron microscopy is used to confirm the layered film structure and hexagonal arrangement of surface atoms. Temperature dependent electrical measurements show an insulating behavior which agrees well with a two-dimensional variable-range hopping model, suggesting that transport in these films is dominated by localized charge-carrier states.

KEYWORDS: Two-dimensional, molybdenum ditelluride, molybdenum diselenide, molecular beam epitaxy, transmission electron microscopy, variable-range hopping.

INTRODUCTION

Semiconducting two-dimensional (2D) transition metal dichalcogenides (TMDs) are being actively investigated as the channel material for post-Si electronic devices.¹⁻³ Their atomically thin nature, coupled with unique physical^{4,5} and optoelectronic properties,⁶⁻⁸ have also enabled exploration of novel spin and valleytronic phenomena.⁹⁻¹¹ To date, most of the studies on TMDs have utilized micrometer sized flakes that are mechanically exfoliated from bulk crystals.¹²⁻¹⁷ While providing a workable platform for proof-of-concept demonstrations, this approach is un-scalable and prevents large scale integration that is crucial for practical TMD-based device architectures. Chemical vapor deposition (CVD) has recently attracted significant attention for pseudo large area growth of TMD thin films.¹⁸⁻²⁰ However, the discontinuous nature of the films, lack of thickness control and homogeneity are its major drawbacks. Moreover, CVD growth has been mostly limited to the light chalcogen based TMDs (sulfides and selenides).

Molecular beam epitaxy (MBE) is a versatile growth technique which is widely used for large area growth of high quality crystalline films and heterostructures. Compared to CVD, MBE offers greater control of film thickness, the ability to incorporate dopants, and the capability to grow high quality heterostructures with abrupt interfaces. In the context of TMDs, weak van der Waal's bonding, and the absence of dangling bonds along the *z*-direction enables their crystalline growth on arbitrary substrates through van der Waal's epitaxy (vdWE). Recent reports on vdWE of molybdenum diselenide (MoSe₂) permitted investigation of its structural and physical properties using transmission electron microscopy (TEM), photoelectron spectroscopy, and scanning tunneling microscopy.^{7,8,21-25} The growth on

conducting graphite substrates has however prevented electrical characterization of these films. Furthermore, heavy chalcogen based TMDs such as molybdenum ditelluride (MoTe_2) with a bandgap closer to Si (~ 1.0 eV) have received lesser attention, with the MBE growth of MoTe_2 being virtually unexplored.

In this work, we report on the structural and electrical properties of large area MoTe_2 and MoSe_2 thin films grown by MBE on $c\text{-Al}_2\text{O}_3(0001)$ (sapphire) substrates. Several *in situ* and *ex situ* characterization techniques are used to confirm the stoichiometry and crystalline nature of the films. Growth on insulating sapphire substrates enables electrical characterization of the as-grown films. Temperature-dependent transport measurements display a trend of increasing resistance with decreasing temperature. The behavior fits well with a 2D Mott variable-range hopping (VRH) mechanism, indicating transport that is dominated by localized charge-carrier states, possibly due to disorder and defects.²⁶

RESULTS AND DISCUSSION

We chose insulating crystalline sapphire substrates due to their hexagonal surface symmetry, and to enable transport measurements of the as-grown films. The growths were done in a custom-built MBE chamber (Omicron systems) with a base pressure of 1×10^{-10} mbar. Single crystal $c\text{-Al}_2\text{O}_3(0001)$ substrates were prepared by resistive heating, and monitored by *in situ* reflection high-energy electron diffraction (RHEED). Thin films of MoTe_2 and MoSe_2 were subsequently grown by co-evaporation of Mo, Te and Mo, Se, respectively. The substrate temperature was 350 °C for MoTe_2 and 250 °C for MoSe_2 . More details of the growth process are described in the Materials and Methods section. Figure 1 shows the RHEED images of the substrates before and after growth. Optical micrographs of the large area, homogeneous ($\sim 6 \times 5$ mm²) films of MoTe_2 and MoSe_2 are shown in Supporting Information S1. The RHEED pattern of the sapphire substrate disappears completely within a few minutes of growth, and a diffused pattern appears, that is indicative of a poly-crystalline film structure (S2 in Supporting Information). Following growth, a high temperature anneal was done at 600 °C for 10 min to improve the crystallinity of the films, resulting in the final sharp, streaky RHEED patterns as shown in Figure 1(b) and (d). The post-growth anneals were performed in a chalcogen rich environment to minimize vacancies due to chalcogen out-diffusion. The MoTe_2 RHEED images show a faint signature of spots along with streaks, possibly due to regions of clustered growth and/or disordered surface regions.²¹ The streaks in the MoSe_2 RHEED images are relatively sharper. We elaborate on this difference in the later sections. Despite the large lattice mismatch with the substrate, the streaky RHEED features suggest well-structured film growth with high crystalline quality and atomically flat surfaces. We also note that the RHEED features are insensitive to both sample and beam orientation.⁷ Furthermore, the growth occurs along the c -axis, as expected for the vdWE growth of a hexagonal thin film on an hcp(0001) substrate. We focus on data from few-layer films in the subsequent sections in order to ensure film continuity and enable electrical characterization.

X-ray diffraction (XRD) was done to evaluate the structure of the films and to confirm their epitaxial nature. Figure 1(e) and (f) show the XRD patterns for a 4 nm film of MoTe_2 and a 5 nm film of MoSe_2 , respectively. Both the patterns show characteristic peaks that correspond to diffraction from the family of (002) planes, as expected for the symmetry group $P6_3/mmc$. The absence of peaks other than the (00 l) family confirms vdWE growth along the c -axis of the sapphire substrates. The sharp peak at $2\theta = 41.7^\circ$ corresponds to reflection from the (006) plane of the sapphire substrate. The peak positions match well with the (00 l) planes of 2H- MoTe_2 (JCPDS No. 73-1650) and 2H- MoSe_2 (JCPDS No. 77-1715).^{27,28} The relatively higher intensity of the (002) peak is a signature of a well-stacked layered structure. It is to be noted that the broadness of the peaks is likely due to the thin-film nature; however, disorder or textured nature of the films cannot be ruled out. The extracted c -axis lattice constants are 13.9 Å for MoTe_2 and 13.0 Å for MoSe_2 , which match closely with the bulk crystal values.^{27,28}

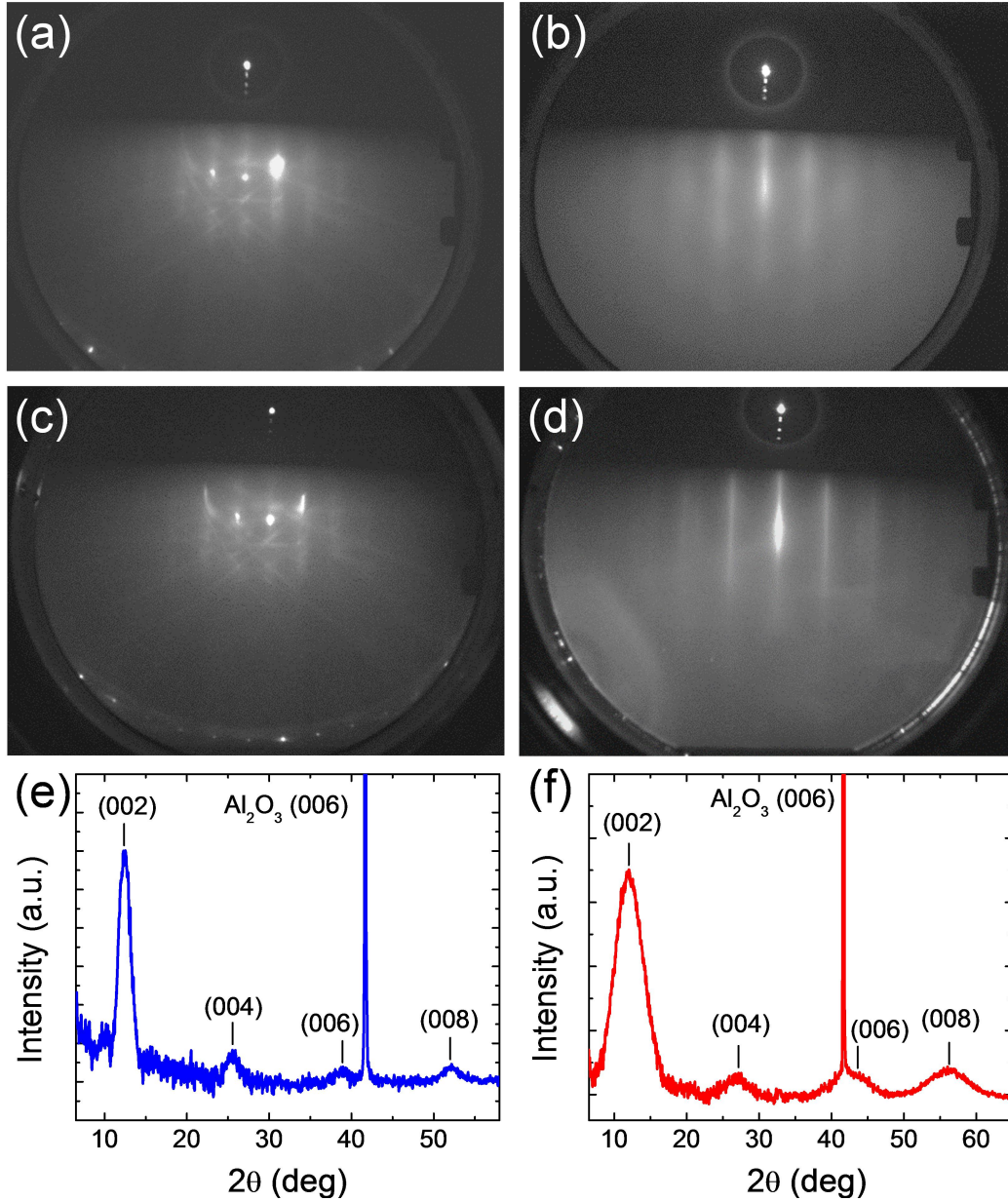


Figure 1 RHEED patterns (a) before and (b) after growth of MoTe₂ on *c*-Al₂O₃(0001) taken along the [1 1 -2 0] direction show streaky features indicative of layered film growth with atomically flat surfaces. The corresponding patterns for MoSe₂ (c, d) show very similar features. The XRD patterns for MoTe₂ (e) and MoSe₂ (f) show peaks characteristic of the 2H polytypes, and confirm growth along the *c*-axis.

The elemental composition and stoichiometry of the films were investigated through X-ray photoelectron spectroscopy (XPS) measurements. Survey spectra of the films (Supporting Information S3) show predominant peaks from Mo and Te/Se, along with weak contribution from Al and O from the sapphire substrate. Figure 2 shows the high-resolution XPS spectra for both MoTe₂ and MoSe₂. It is to be noted that the O contribution is only from the substrate, as evident from the absence of oxide doublets in the high-resolution spectra. The binding energies of Mo-3*d*_{5/2} (227.8 eV) and Mo-3*d*_{3/2} (230.9 eV) in Figure 2(a) are consistent with the +4 oxidation state of Mo. Similarly, Te-3*d*_{5/2} (572.4 eV) and Te-3*d*_{3/2} (582.8 eV) in Figure 2(b) correspond to the -2 oxidation state of Te. There is a close agreement of the

peak positions with reported values for 2H-MoTe₂ bulk crystals.²⁹ Absence of Mo and Te peaks of other oxidation states confirms homogeneity of the 2H phase to within the detection limit. Using the integrated peak areas of Mo-3d and Te-3d, we obtain a Te:Mo ratio of 1.91. The deviation from the expected stoichiometric value of 2 for 2H-MoTe₂ could be due to the presence of disorder possibly from chalcogen vacancies, and/or the presence of other polytypes. The energy difference ΔE between Mo-3d_{5/2} and Te-3d_{5/2} in MoTe₂ is 344.7 eV, which is very close to that of the corresponding elemental peaks (345.2 eV).²⁹ This is due to the small electronegativity difference between Mo and Te ($\Delta\chi_{\text{Te-Mo}} = 0.3$). As a result, the bonding energy of MoTe₂ is lower compared to other Mo based TMDs, and can therefore lead to a higher incidence of Te vacancies. Figure 2(c) and (d) show the corresponding high-resolution XPS spectra of Mo and Se, respectively, in MoSe₂. While the Mo spectrum is similar to that of MoTe₂, the Se-3d doublet is not as well resolved as the Te-3d doublet. This is due to the lower atomic mass of Se which results in a lower spin splitting of Se-3d compared to Te-3d. A Se:Mo ratio of 1.95 is extracted for the MoSe₂. The slight deviation from the stoichiometric value of 2 could be due to Se vacancies, similar to Te vacancies in MoTe₂. The bonding energy between Mo and Se is higher than Mo and Te, as evident from the $\Delta E = 174.4$ eV between Mo-3d_{5/2} and Se-3d_{5/2} in MoSe₂, compared to 172.4 eV between elemental Mo and Se.³⁰ A closer to ideal stoichiometry in MoSe₂ compared to MoTe₂ is due to the stronger Mo-Se bonds. The weaker Mo-Te bonds are also responsible for the higher prevalence of disorder in MoTe₂, as apparent in the RHEED patterns of Figure 1.

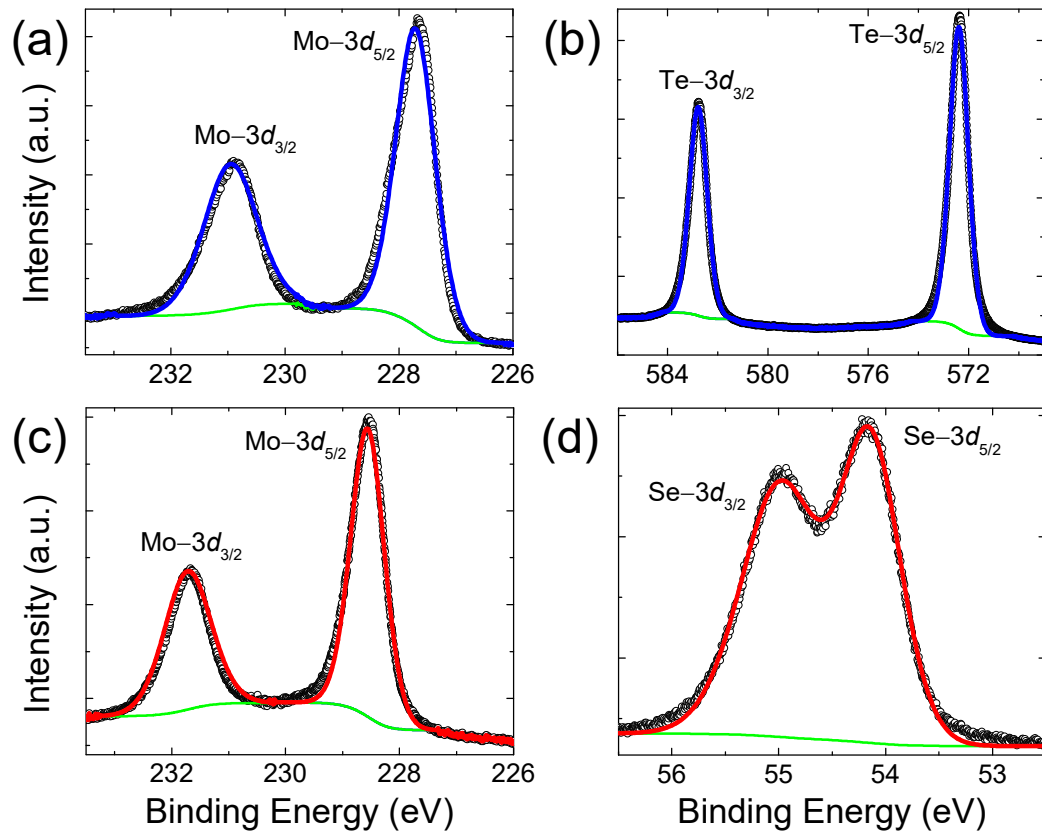


Figure 2 The high-resolution XPS spectra of MoTe₂ and MoSe₂ thin films. (a) Mo-3d and (b) Te-3d core level peaks of MoTe₂ and (c) Mo-3d and (d) Se-3d core level peaks of MoSe₂ show chemical shifts corresponding to homogeneous phases of 2H-MoTe₂ and 2H-MoSe₂, respectively. An Mo:Te ratio of 1.91 and Mo:Se ratio of 1.95 is extracted from the area fit (solid lines) to the experimental data (circles).

Figure 3(a) and (b) show Raman spectra of the MoTe₂ and MoSe₂ films, respectively. Spectra from exfoliated bulk flakes on Si/SiO₂ substrates are also shown for comparison. The measurements were done using a 532 nm laser. Group theory analysis for bulk TMDs (belonging to the D_{6h} group) predicts four Raman-active and two Raman-inactive modes.³¹ Out of the four Raman-active modes, E_{1g}, E¹_{2g} and E²_{2g} arise from the in-plane Raman-active vibrations, and A_{1g} is due to the out-of-plane vibrations. In addition, the Raman-inactive breathing mode B¹_{2g} becomes active in few-layer 2H-TMDs, due to the breaking of crystal symmetry along the *c*-axis.³² Both MoTe₂ and MoSe₂ show prominent E¹_{2g} (MoTe₂: 236.1 cm⁻¹ and MoSe₂: 286.4 cm⁻¹) and A_{1g} (MoTe₂: 173.9 cm⁻¹ and MoSe₂: 245.5 cm⁻¹) peaks, reaffirming the crystalline layered structure of our films. The positions and relative intensities of both peaks match very well with that of the corresponding exfoliated flakes, as well as previous literature reports.^{22,32} The broadening of the peaks in our MBE films compared to exfoliated flakes could be due to defects arising from chalcogen vacancies and/or grain structure which can cause localization of phonons.²² In addition, we observe the E_{1g} peak (MoTe₂: 107.1 cm⁻¹ and MoSe₂: 172.8 cm⁻¹) in both our MBE films. While this peak is absent in exfoliated MoTe₂, there is a faint signature in exfoliated MoSe₂. However, Kan *et al.*³³ have shown from density-functional calculations that a stable E_{1g} mode does exist around 110 cm⁻¹ for 2H-MoTe₂. Further, the existence of the B¹_{2g} peaks (MoTe₂: 282.4 cm⁻¹ and MoSe₂: 354.3 cm⁻¹) indicates that our films are few-layer thick. The unlabeled peak at around 138 cm⁻¹ in MoTe₂ could be a second-order Raman mode that is observed even in the exfoliated flake, and in prior reports.^{15,32} Figure 3(c) shows the photoluminescence (PL) spectrum of the MoSe₂ film. The characteristic peak at 1.55 eV corresponds to the direct band-gap transition of few-layer MoSe₂, as reported in literature.³⁴ The ultraviolet-visible (UV-Vis) absorption spectrum of MoSe₂ also shows a band-gap close to 1.58 eV (Supporting Information S4). The corresponding PL peak of MoTe₂ (~ 0.9 eV) was beyond the measurement window of our setup.

Transmission Electron Microscopy (TEM) was done to evaluate the micro-structure of the films. Plan-view TEM was employed to study the surface lattice arrangement of atoms, and cross-sectional TEM (X-TEM) for investigation of the film-substrate interface,

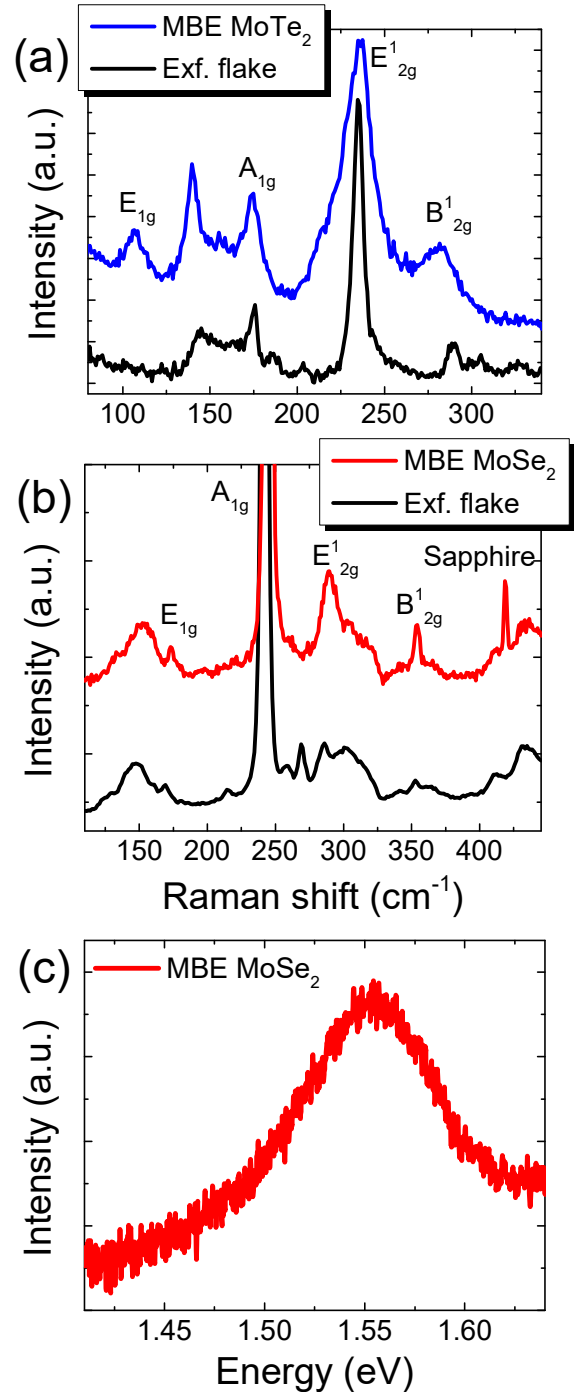


Figure 3 (a) The Raman spectrum of a 5 nm MoTe₂ film (in blue) matches well with the corresponding spectrum of an exfoliated few-layer 2H-MoTe₂ flake (in black). The slightly broader peaks in the MBE film could be due to defects. (b) The Raman spectrum of a 5 nm MoSe₂ film (in red) and an exfoliated few-layer 2H-MoSe₂ flake (in black) also match closely. (c) The PL spectrum of MoSe₂ shows a characteristic peak at ~ 1.55 eV.

and layer structure. For plan-view TEM, the films were transferred onto a holey carbon grid using a wet transfer technique. Low-magnification X-TEM images along the $\langle 0110 \rangle$ direction show uniform film growth without discontinuities or pinholes, with a thickness around 4-5 nm for both MoTe_2 and MoSe_2 (Supporting Information S5).

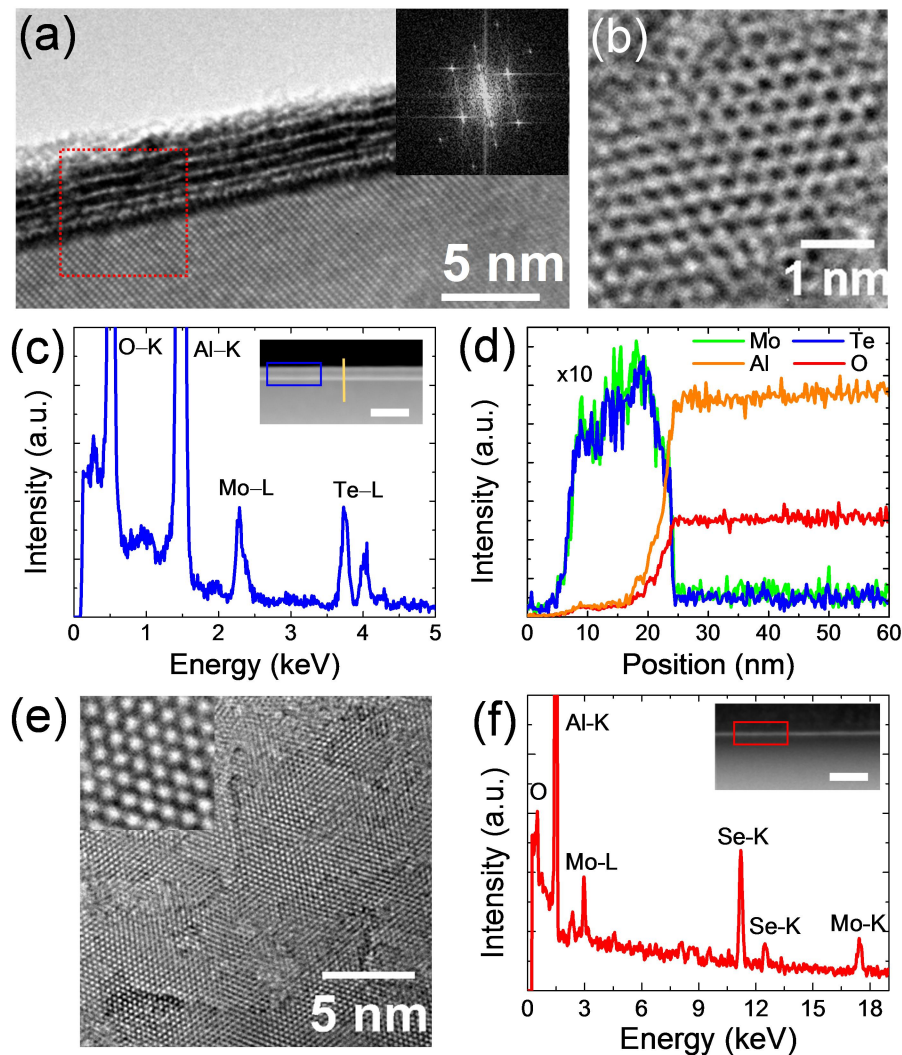


Figure 4 (a) High-resolution X-TEM image of MoTe_2 shows the layer structure confirming vdWE growth. The inset shows the fast Fourier transform of the region marked in red. (b) The plan-view TEM image of MoTe_2 shows the hexagonal arrangement of surface atoms. (c) The EDX area spectrum acquired from the STEM image (inset) shows signals from the constituent elements. (d) The EDX line spectrum acquired along the line marked in the inset of (c). (e) Plan-view TEM image of MoSe_2 shows its hexagonal lattice (zoomed in view in the inset is $2 \times 2 \text{ nm}^2$). (f) The EDX area spectrum of MoSe_2 shows contribution from the region marked in the inset.

Figure 4(a) shows a representative high-resolution X-TEM (HR-XTEM) image for a 4 nm MoTe_2 film. The distinct layered structure of MoTe_2 is apparent, along with its abrupt interface with the sapphire substrate. The interlayer spacing of $\sim 7 \text{ \AA}$ agrees closely with the bulk MoTe_2 spacing.²⁷ The contrast variation in the layer closest to the substrate could be attributed to strain relaxation in the MoTe_2 . The presence of grain boundaries and dislocations could be the reason for contrast variations in the layers further from the interface. The inset of Figure 4(a) shows the fast Fourier transform pattern obtained from

the area marked in red, which highlights the hexagonal crystal structure and epitaxial relation between the film and the substrate. The hexagonal lattice arrangement of atoms is shown in the plan-view TEM image in Figure 4(b). The lattice constant ($a = 3.5 \text{ \AA}$) extracted from the plan-view TEM micrographs matches with that of bulk 2H-MoTe₂.²⁷ Plan-view TEM images of a larger area show the presence of grains and defects (Supporting Information S6). However, considering the possibility of film damage during transfer onto the TEM grid, it is difficult to precisely comment on the origin of these grains and defects. Similar grain structure has been observed in previous reports of MBE MoSe₂ films and been attributed to the low mobility of Mo on *c*-Al₂O₃(0001) surfaces.^{22,35} Figure 4(c) and (d) show the energy dispersive x-ray spectroscopy (EDX) scans of the MoTe₂ film from the marked regions of the scanning transmission electron microscopy (STEM) image shown in the inset of Figure 4(c). The EDX spectrum from the area highlighted in blue shows peaks corresponding to Mo, Te (from the MoTe₂ film) and Al, O (from the sapphire substrate). Figure 4(d) shows the EDX profile along the red line marked in the inset of Figure 4(c). The signals from Mo and Te show the highest intensity at the location corresponding to the MoTe₂ film, and fall abruptly away from the film. Signals from Al and O dominate in the regions away from the MoTe₂ film. An atomic percentage ratio of Mo:Te $\sim 1:1.86$ is extracted from the EDX spectrum, which is consistent with the ratio calculated from *in situ* XPS analysis. Figure 4(e) shows the plan-view TEM image of MoSe₂. The lattice arrangement of atoms is hexagonal throughout the image (as shown in a zoomed-in view in the inset), albeit with the existence of defects and grains. The extracted lattice constant of 3.3 \AA matches well with the bulk 2H-MoSe₂, and the interlayer spacing is $\sim 6.7 \text{ \AA}$ (Supporting Information S6), which agrees well with the data obtained from XRD.²⁸ Figure 4(f) shows the EDX spectrum of the region marked in the inset, which gives an Mo:Se ratio of $\sim 1:1.94$.

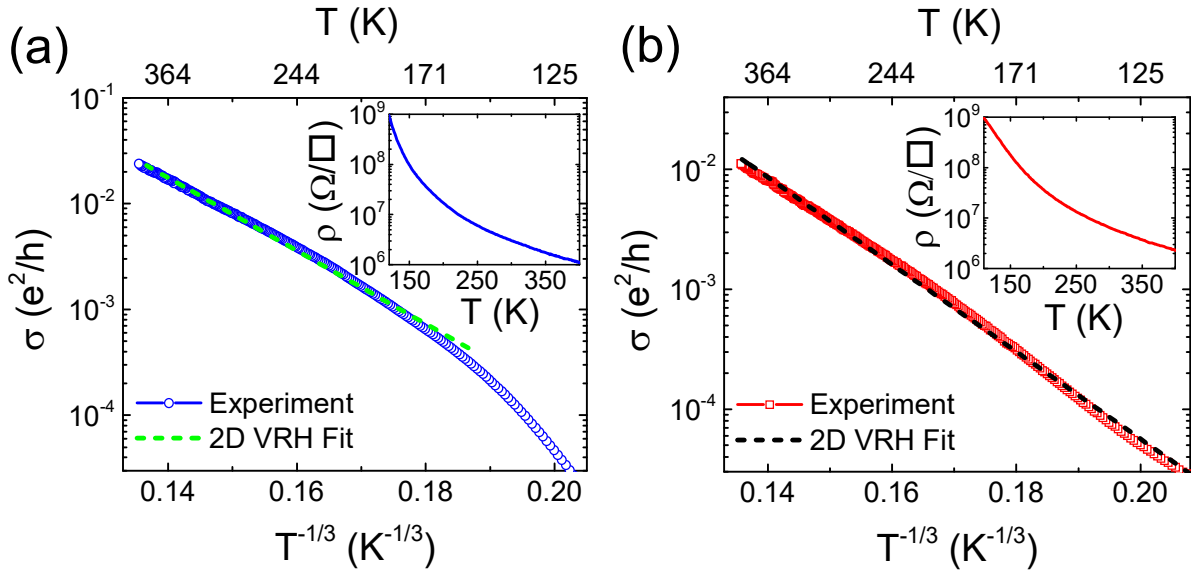


Figure 5 Electrical transport measurements of (a) MoTe₂ and (b) MoSe₂. The variation of conductivity on a semi-log scale vs $T^{-1/3}$ follows a linear trend which can be fit to a 2D Mott VRH transport model (dotted lines). The temperature dependence of the measured resistivities (shown in the insets) follow an insulating trend.

We now move on to electrical characterization of the films. The large-area continuous nature of the films, and the insulating sapphire substrate enabled us to perform temperature-dependent resistivity measurements of the as-grown films using a four-point probe geometry. Both the MoTe₂ and MoSe₂ showed a similar insulating behavior i.e., resistivity increasing with decreasing temperature (insets of Figure 5(a) and (b)). The data was initially fit with an Arrhenius law dependence, $\sigma \propto e^{-E_a/k_B T}$, where σ is the conductivity, E_a is the thermal activation energy, k_B is the Boltzmann constant, and T is the

temperature. A poor fit, and unreasonably low values of E_a for both the films (Supporting Information S7) indicate that the transport is likely to be dominated by a different physical transport mechanism. We therefore consider a 2D Mott variable-range hopping (VRH) mechanism to describe the transport in our films. Transport mediated by VRH is commonly observed in semiconducting films with a predominance of localized charge-carrier states.^{26,36,37} The temperature dependence of σ in VRH follows

$$\sigma(T) \propto \exp \left[- \left(\frac{T_0}{T} \right)^{1/3} \right]$$

where, T_0 is a fitting parameter, and the exponent 1/3 is characteristic to 2D transport. The 2D VRH model has been used to describe transport in disordered TMDs in several prior literature reports.^{15,26,38} Figure 5(a) and (b) show the normalized conductance on a semi-log scale plotted with respect to $T^{1/3}$, for MoTe₂ and MoSe₂, respectively. The linear dependence confirms that the conduction in our films is indeed dominated by a VRH mechanism. We note that the fit for MoTe₂ is over a smaller temperature range compared to MoSe₂. The extracted values of T_0 are 4.95×10^5 K for MoTe₂ and 5.88×10^5 K for MoSe₂. The high values of T_0 compared to values reported^{26,39} for MoS₂ indicate a higher degree of carrier localization, possibly stemming from disorder due to chalcogen vacancies, and/or the grainy structure of our films. The VRH behavior in our films is likely due to intrinsic short-range structural disorder.^{26,39} The higher values of T_0 also imply a smaller localization length (ζ), which impedes charge carriers to hop across localized states. This high degree of localization can lead to VRH type transport even at room temperature.³⁶ The observation of VRH mediated transport in our films concurs with the existence of grains and defects as manifested in the TEM images. Furthermore, the sensitivity of the top few layers to oxygen and moisture, more so in the case of MoTe₂, can exacerbate the pre-existing disorder and affect the transport in the films.⁴⁰

CONCLUSION

In conclusion, we have carried out the MBE growth of MoTe₂ and MoSe₂ thin films on insulating *c*-Al₂O₃(0001) substrates. *In situ* characterization using RHEED showed sharp streaky features indicative of atomically flat films grown *via* a vdWE growth mechanism. The film stoichiometry and chemical composition were investigated through *in situ* XPS measurements, and revealed homogeneous phases of MoTe₂ and MoSe₂, albeit being slightly chalcogen deficient. XRD measurements showed peaks characteristic of the 2H polytypes for both MoTe₂ and MoSe₂, and further confirmed growth along the *c*-axis of the films. Raman spectroscopy measurements on the grown films match closely with the corresponding bulk flakes, highlighting their crystalline quality. Cross-sectional and plan-view TEM measurements were used to conclusively determine the layer structure and hexagonal arrangement of surface atoms. Finally, electrical measurements on the as-grown films showed an insulating behavior, which was found to follow a 2D Mott variable-range hopping mechanism, suggestive of localized charge carrier states arising from disorder.

The large difference in vapor pressures between Mo and the chalcogen species severely tightens the growth window, in turn translating to a high propensity for chalcogen defects and a diminished grain size.²⁵ The resulting disorder in the films is apparent from both the TEM images and transport measurements. Our results suggest that despite their seemingly promising spectroscopic quality, MBE-grown TMDs on sapphire may be prone to microscopic defects and disorder, which degrade their electrical characteristics. The choice of substrate, growth conditions, and post-growth treatment play a major role on the film quality, and therefore merit further investigation.

MATERIALS AND METHODS

Growth: The growth was done in a custom-built MBE growth chamber (Omicron, Germany) under ultra-high vacuum (UHV) conditions (base pressure $\sim 1 \times 10^{-10}$ mbar). Details of the system have been described elsewhere.⁴¹ After pre-cleaning in acetone and isopropanol, the insulating *c*-Al₂O₃(0001) substrates were introduced into the UHV chamber and prepared by resistive heating at 600 °C for 3 hours followed by 700 °C for 30 min, and monitored *in situ* by RHEED. Molybdenum and tellurium (selenium) fluxes generated by an *e*-beam evaporator and an effusion cell (hot lip Knudsen, NTEZ, Scienta Omicron), respectively, were co-deposited onto the substrates at a substrate temperature of 350 °C (250 °C). The chamber pressure during growth never exceeded 1×10^{-9} mbar and the Te₂/Mo (Se₂/Mo) beam equivalent pressure (BEP) flux ratio was kept around 15. The growth was followed by a post-deposition *in situ* anneal at 600 °C for 10 min with the chalcogen flux ON, which resulted in greatly improved streak features in RHEED. Several samples with thicknesses varying from 3 nm to 10 nm were grown with typical growth rates around 0.1 nm/min.

Characterization: Post-growth investigations were carried out by *in situ* RHEED operated at 13 kV, and XPS with a monochromatic Al-K α source ($h\nu = 1486.7$ eV) operating at 15 kV. A Renishaw inVia Raman microscope with a 532 nm diode laser was used for the *ex situ* Raman (3600 *l/mm*) and PL (1200 *l/mm*) measurements. A Philips X-Pert XRD system equipped with a Cu X-ray filament source and a PW-3011/20 proportional detector was used for the XRD measurements. The TEM images were taken using FEI-Tecna TF30 and TF20 microscopes. The plan-view TEM samples were prepared by transferring the as-grown film onto holey carbon TEM grids using a poly(methyl methacrylate)-based wet-transfer technique, by detaching the films from the sapphire substrate using an NaOH etch.

Electrical Measurements: The as-grown samples were contacted at the four corners using indium dots to perform four-point measurements. Temperature dependent measurements were performed in a Lakeshore CPX probe-station using an Agilent B1500A parameter analyzer. The measurements were done in a constant current mode, with a dc excitation current of 5 nA.

Conflict of interest: The authors declare no competing financial interest.

Acknowledgment: This work was supported in part by NRI SWAN and NSF NNCI. We appreciate technical support from Omicron.

Supporting Information Available: S1: Large-area MBE Growth, S2: Effect of Annealing: Evolution of RHEED, S3: X-ray Photoelectron Spectroscopy Survey Scan, S4: UV-Vis Absorption Spectroscopy, S5: X-TEM of MoTe₂ and MoSe₂, S6: Plan-view TEM of MoTe₂ and MoSe₂, S7: Arrhenius Fit to Electrical Data.

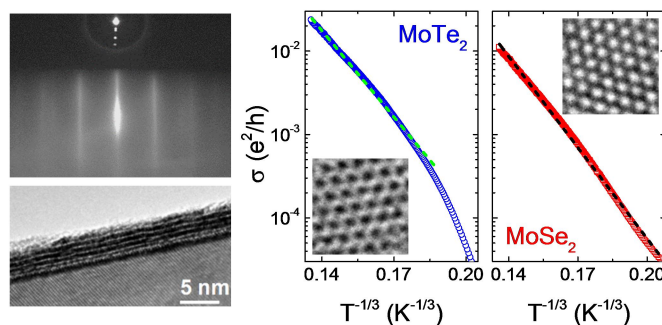
REFERENCES

- (1) Jariwala, D.; Sangwan, V. K.; Lauhon, L. J.; Marks, T. J.; Hersam, M. C. Emerging Device Applications for Semiconducting Two-Dimensional Transition Metal Dichalcogenides. *ACS Nano* **2014**, *8* (2), 1102–1120.
- (2) Wang, Q. H.; Kalantar-Zadeh, K.; Kis, A.; Coleman, J. N.; Strano, M. S. Electronics and Optoelectronics of Two-Dimensional Transition Metal Dichalcogenides. *Nat Nano* **2012**, *7* (11), 699–712.
- (3) Chhowalla, M.; Shin, H. S.; Eda, G.; Li, L.-J.; Loh, K. P.; Zhang, H. The Chemistry of Two-Dimensional Layered Transition Metal Dichalcogenide Nanosheets. *Nat Chem* **2013**, *5* (4), 263–275.
- (4) Lee, G.-H.; Yu, Y.-J.; Cui, X.; Petrone, N.; Lee, C.-H.; Choi, M. S.; Lee, D.-Y.; Lee, C.; Yoo, W. J.; Watanabe, K.; Taniguchi, T.; Nuckolls, C.; Kim, P.; Hone, J. Flexible and Transparent MoS₂ Field-Effect Transistors on Hexagonal Boron Nitride-Graphene Heterostructures. *ACS Nano* **2013**, *7* (9), 7931–7936.
- (5) Bernardi, M.; Palummo, M.; Grossman, J. C. Extraordinary Sunlight Absorption and One Nanometer Thick Photovoltaics Using Two-Dimensional Monolayer Materials. *Nano Lett.* **2013**, *13* (8), 3664–3670.
- (6) Mak, K. F.; Lee, C.; Hone, J.; Shan, J.; Heinz, T. F. Atomically Thin MoS₂: A New Direct-Gap Semiconductor. *Phys. Rev. Lett.* **2010**, *105* (13), 136805.

- (7) Zhang, Y.; Chang, T.-R.; Zhou, B.; Cui, Y.-T.; Yan, H.; Liu, Z.; Schmitt, F.; Lee, J.; Moore, R.; Chen, Y.; Lin, H.; Jeng, H.-T.; Mo, S.-K.; Hussain, Z.; Bansil, A.; Shen, Z.-X. Direct Observation of the Transition from Indirect to Direct Bandgap in Atomically Thin Epitaxial MoSe₂. *Nat Nano* **2014**, *9* (2), 111–115.
- (8) Ugeda, M. M.; Bradley, A. J.; Shi, S.-F.; da Jornada, F. H.; Zhang, Y.; Qiu, D. Y.; Ruan, W.; Mo, S.-K.; Hussain, Z.; Shen, Z.-X.; Wang, F.; Louie, S. G.; Crommie, M. F. Giant Bandgap Renormalization and Excitonic Effects in a Monolayer Transition Metal Dichalcogenide Semiconductor. *Nat Mater* **2014**, *13* (12), 1091–1095.
- (9) Mak, K. F.; McGill, K. L.; Park, J.; McEuen, P. L. The Valley Hall Effect in MoS₂ Transistors. *Science* **2014**, *344* (6191), 1489–1492.
- (10) Xu, X.; Yao, W.; Xiao, D.; Heinz, T. F. Spin and Pseudospins in Layered Transition Metal Dichalcogenides. *Nat Phys* **2014**, *10* (5), 343–350.
- (11) Xiao, D.; Liu, G.-B.; Feng, W.; Xu, X.; Yao, W. Coupled Spin and Valley Physics in Monolayers of MoS₂ and Other Group-VI Dichalcogenides. *Phys. Rev. Lett.* **2012**, *108* (19), 196802.
- (12) Das, S.; Chen, H.-Y.; Penumatcha, A. V.; Appenzeller, J. High Performance Multilayer MoS₂ Transistors with Scandium Contacts. *Nano Lett.* **2013**, *13* (1), 100–105.
- (13) McDonnell, S.; Addou, R.; Buie, C.; Wallace, R. M.; Hinkle, C. L. Defect-Dominated Doping and Contact Resistance in MoS₂. *ACS Nano* **2014**, *8* (3), 2880–2888.
- (14) Larentis, S.; Fallahzad, B.; Tutuc, E. Field-Effect Transistors and Intrinsic Mobility in Ultra-Thin MoSe₂ Layers. *Appl. Phys. Lett.* **2012**, *101* (22), 223104.
- (15) Pradhan, N. R.; Rhodes, D.; Feng, S.; Xin, Y.; Memaran, S.; Moon, B.-H.; Terrones, H.; Terrones, M.; Balicas, L. Field-Effect Transistors Based on Few-Layered α -MoTe₂. *ACS Nano* **2014**, *8* (6), 5911–5920.
- (16) Legma, J. B.; Vacquier, G.; Casalot, A. Chemical Vapour Transport of Molybdenum and Tungsten Diselenides by Various Transport Agents. *J. Cryst. Growth* **1993**, *130* (1–2), 253–258.
- (17) Lezama, I. G.; Ubaldini, A.; Longobardi, M.; Giannini, E.; Renner, C.; Kuzmenko, A. B.; Morpurgo, A. F. Surface Transport and Band Gap Structure of Exfoliated 2H-MoTe₂ Crystals. *2D Mater.* **2014**, *1* (2), 021002.
- (18) Lee, Y.-H.; Zhang, X.-Q.; Zhang, W.; Chang, M.-T.; Lin, C.-T.; Chang, K.-D.; Yu, Y.-C.; Wang, J. T.-W.; Chang, C.-S.; Li, L.-J.; Lin, T.-W. Synthesis of Large-Area MoS₂ Atomic Layers with Chemical Vapor Deposition. *Adv. Mater.* **2012**, *24* (17), 2320–2325.
- (19) Wang, X.; Gong, Y.; Shi, G.; Chow, W. L.; Keyshar, K.; Ye, G.; Vajtai, R.; Lou, J.; Liu, Z.; Ringe, E.; Tay, B. K.; Ajayan, P. M. Chemical Vapor Deposition Growth of Crystalline Monolayer MoSe₂. *ACS Nano* **2014**, *8* (5), 5125–5131.
- (20) Zhou, L.; Xu, K.; Zubair, A.; Liao, A. D.; Fang, W.; Ouyang, F.; Lee, Y.-H.; Ueno, K.; Saito, R.; Palacios, T.; Kong, J.; Dresselhaus, M. S. Large-Area Synthesis of High-Quality Uniform Few-Layer MoTe₂. *J. Am. Chem. Soc.* **2015**, *137* (37), 11892–11895.
- (21) Xenogiannopoulou, E.; Tsipas, P.; Aretouli, K. E.; Tsoutsou, D.; Giamini, S. A.; Bazioti, C.; Dimitrakopoulos, G. P.; Komninou, P.; Brems, S.; Huyghebaert, C.; Radu, I. P.; Dimoulas, A. High-Quality, Large-Area MoSe₂ and MoSe₂/Bi₂Se₃ Heterostructures on AlN(0001)/Si(111) Substrates by Molecular Beam Epitaxy. *Nanoscale* **2015**, *7* (17), 7896–7905.
- (22) Vishwanath, S.; Liu, X.; Rouvimov, S.; Mende, P. C.; Azcatl, A.; McDonnell, S.; Wallace, R. M.; Feenstra, R. M.; Furdyna, J. K.; Jena, D.; Xing, H. G. Comprehensive Structural and Optical Characterization of MBE Grown MoSe₂ on Graphite, CaF₂ and Graphene. *2D Mater.* **2015**, *2* (2), 024007.
- (23) Lehtinen, O.; Komsa, H.-P.; Pulkin, A.; Whitwick, M. B.; Chen, M.-W.; Lehnert, T.; Mohn, M. J.; Yazyev, O. V.; Kis, A.; Kaiser, U.; Krasheninnikov, A. V. Atomic Scale Microstructure and Properties of Se-Deficient Two-Dimensional MoSe₂. *ACS Nano* **2015**, *9* (3), 3274–3283.
- (24) Liu, H.; Zheng, H.; Yang, F.; Jiao, L.; Chen, J.; Ho, W.; Gao, C.; Jia, J.; Xie, M. Line and Point Defects in MoSe₂ Bilayer Studied by Scanning Tunneling Microscopy and Spectroscopy. *ACS Nano* **2015**, *9* (6), 6619–6625.
- (25) Jiao, L.; Liu, H. J.; Chen, J. L.; Yi, Y.; Chen, W. G.; Cai, Y.; Wang, J. N.; Dai, X. Q.; Wang, N.; Ho, W. K.; Xie, M. H. Molecular-Beam Epitaxy of Monolayer MoSe₂: Growth Characteristics and Domain Boundary Formation. *New J. Phys.* **2015**, *17* (5), 053023.
- (26) Ghatak, S.; Pal, A. N.; Ghosh, A. Nature of Electronic States in Atomically Thin MoS₂ Field-Effect Transistors. *ACS Nano* **2011**, *5* (10), 7707–7712.
- (27) Knop, O.; MacDonald, R. D. Chalcogenides of the Transition Elements: III. Molybdenum Ditelluride. *Can. J. Chem.* **1961**, *39* (4), 897–904.
- (28) James, P.; Lavik, M. The Crystal Structure of MoSe₂. *Acta Crystallogr.* **1963**, *16* (11), 1183–1183.

- (29) Bernède, J.; Amory, C.; Assmann, L.; Spiesser, M. X-Ray Photoelectron Spectroscopy Study of MoTe₂ Single Crystals and Thin Films. *Appl. Surf. Sci.* **2003**, *219* (3–4), 238–248.
- (30) Abdallah, W.; Nelson, A. E. Characterization of MoSe₂(0001) and Ion-Sputtered MoSe₂ by XPS. *J. Mater. Sci.* **2005**, *40* (9–10), 2679–2681.
- (31) Terrones, H.; Corro, E. D.; Feng, S.; Poumirol, J. M.; Rhodes, D.; Smirnov, D.; Pradhan, N. R.; Lin, Z.; Nguyen, M. A. T.; Elías, A. L.; Mallouk, T. E.; Balicas, L.; Pimenta, M. A.; Terrones, M. New First Order Raman-Active Modes in Few Layered Transition Metal Dichalcogenides. *Sci. Rep.* **2014**, *4*, 4215.
- (32) Yamamoto, M.; Wang, S. T.; Ni, M.; Lin, Y.-F.; Li, S.-L.; Aikawa, S.; Jian, W.-B.; Ueno, K.; Wakabayashi, K.; Tsukagoshi, K. Strong Enhancement of Raman Scattering from a Bulk-Inactive Vibrational Mode in Few-Layer MoTe₂. *ACS Nano* **2014**, *8* (4), 3895–3903.
- (33) Kan, M.; Nam, H. G.; Lee, Y. H.; Sun, Q. Phase Stability and Raman Vibration of the Molybdenum Ditelluride (MoTe₂) Monolayer. *Phys. Chem. Chem. Phys.* **2015**, *17* (22), 14866–14871.
- (34) Tongay, S.; Zhou, J.; Ataca, C.; Lo, K.; Matthews, T. S.; Li, J.; Grossman, J. C.; Wu, J. Thermally Driven Crossover from Indirect toward Direct Bandgap in 2D Semiconductors: MoSe₂ versus MoS₂. *Nano Lett.* **2012**, *12* (11), 5576–5580.
- (35) Vishwanath, S.; Rouvimov, S.; Orlova, T.; Liu, X.; Furdyna, J. K.; Jena, D.; Grace Xing, H. Atomic Structure of Thin MoSe₂ Films Grown by Molecular Beam Epitaxy. *Microsc. Microanal.* **2014**, *20* (Supplement S3), 164–165.
- (36) Gómez-Navarro, C.; Weitz, R. T.; Bittner, A. M.; Scolari, M.; Mews, A.; Burghard, M.; Kern, K. Electronic Transport Properties of Individual Chemically Reduced Graphene Oxide Sheets. *Nano Lett.* **2007**, *7* (11), 3499–3503.
- (37) Jariwala, D.; Sangwan, V. K.; Late, D. J.; Johns, J. E.; Dravid, V. P.; Marks, T. J.; Lauhon, L. J.; Hersam, M. C. Band-like Transport in High Mobility Unencapsulated Single-Layer MoS₂ Transistors. *Appl. Phys. Lett.* **2013**, *102* (17), 173107.
- (38) Utama, M. I. B.; Lu, X.; Zhan, D.; Ha, S. T.; Yuan, Y.; Shen, Z.; Xiong, Q. Etching-Free Patterning Method for Electrical Characterization of Atomically Thin MoSe₂ Films Grown by Chemical Vapor Deposition. *Nanoscale* **2014**, *6* (21), 12376–12382.
- (39) Qiu, H.; Xu, T.; Wang, Z.; Ren, W.; Nan, H.; Ni, Z.; Chen, Q.; Yuan, S.; Miao, F.; Song, F.; Long, G.; Shi, Y.; Sun, L.; Wang, J.; Wang, X. Hopping Transport through Defect-Induced Localized States in Molybdenum Disulphide. *Nat Commun* **2013**, *4*, 2642.
- (40) Chen, B.; Sahin, H.; Suslu, A.; Ding, L.; Bertoni, M. I.; Peeters, F. M.; Tongay, S. Environmental Changes in MoTe₂ Excitonic Dynamics by Defects-Activated Molecular Interaction. *ACS Nano* **2015**, *9* (5), 5326–5332.
- (41) Roy, A.; Guchhait, S.; Sonde, S.; Dey, R.; Pramanik, T.; Rai, A.; Movva, H. C. P.; Colombo, L.; Banerjee, S. K. Two-Dimensional Weak Anti-Localization in Bi₂Te₃ Thin Film Grown on Si(111)-(7×7) Surface by Molecular Beam Epitaxy. *Appl. Phys. Lett.* **2013**, *102* (16), 163118.

Figure TOC



Supporting Information

S1: Large-area MBE Growth

Figure S1 shows optical micrographs of the large-area MBE grown MoTe₂ and MoSe₂ thin films on sapphire substrates. The thicknesses of the MoTe₂ and MoSe₂ films are about 5 nm and 7 nm, respectively. The two transparent stripes on the vertical edges correspond to the sample holder clamps, and therefore have no growth.

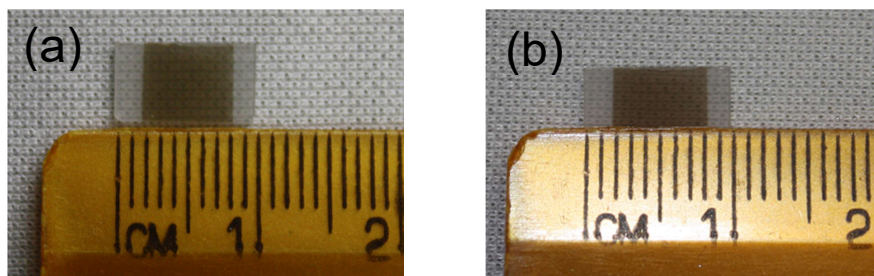


Figure S1 Optical micrographs of MBE grown (a) MoTe₂ and (b) MoSe₂ thin films on sapphire.

S2: Effect of Annealing: Evolution of RHEED

The as-grown MoTe₂ and MoSe₂ films showed diffused RHEED features. A post-growth anneal was done to improve the film quality. Figure S2 shows the RHEED images before and after annealing at 600 °C for 10 min in a chalcogen rich environment. There is a marked improvement in the sharpness and streakiness for both MoTe₂ and MoSe₂, indicating an atomically flat surface morphology. The high temperature anneal increases the surface diffusion of atoms and the presence of a chalcogen flux ensures healing of defects arising from vacancies.¹ The films grow along the *c*-axis of the substrate as should be the case for van der Waal's epitaxy.

S3: X-ray Photoelectron Spectroscopy Survey Scan

Figure S3(a) and (b) show the *in situ* XPS survey scans of the MoTe₂ and MoSe₂ thin films, respectively. All the major peaks have been identified and assigned to Mo, Te (Se). The C-1s peak from the substrate holder was used to calibrate the peak positions.

S4: UV-Vis Absorption Spectroscopy

Room temperature ultraviolet-visible (UV-Vis) absorption spectroscopy has been conducted on a 5 nm MoSe₂ thin film. The data was taken using a Cary 5000 UV-Vis NIR spectrometer. Figure S4 shows the absorbance spectrum as a function of wavelength. The two absorption peaks at 786 nm and 697 nm correspond to the two exciton peaks of MoSe₂, A and B, respectively, originating from the interband exciton transitions at the K-point of the Brillouin zone.²

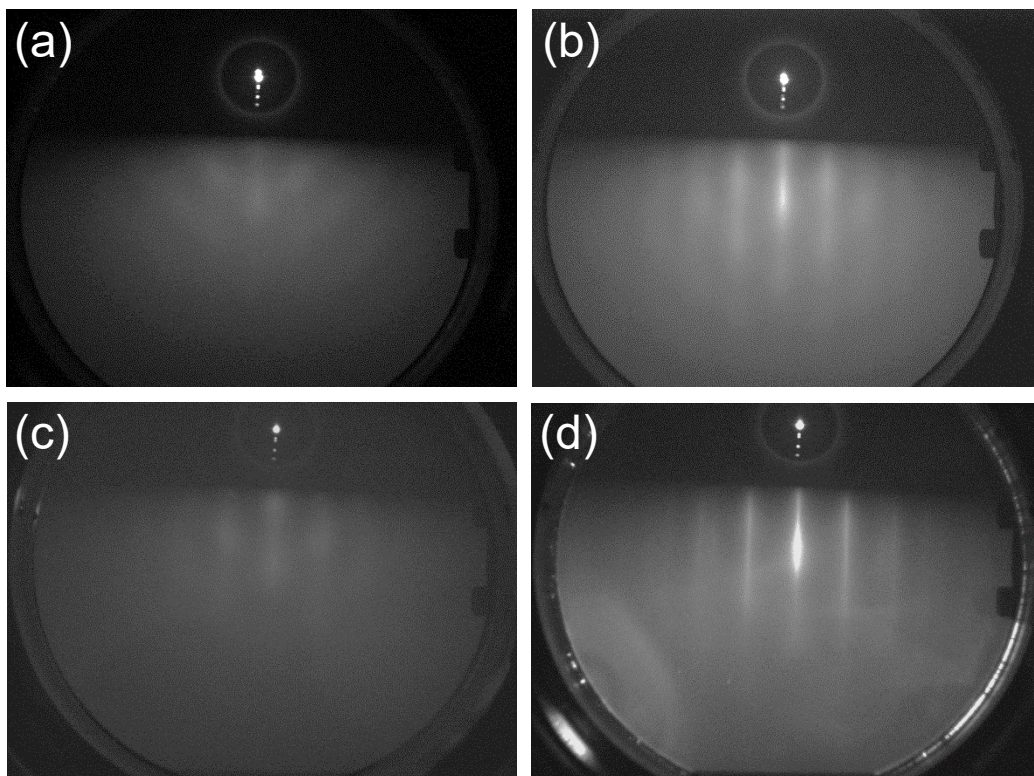


Figure S2 RHEED patterns along the $[1\ 1\ -2\ 0]$ direction of sapphire: from as-grown MoTe_2 and MoSe_2 thin films (a, c) before and (b, d) after annealing, respectively.

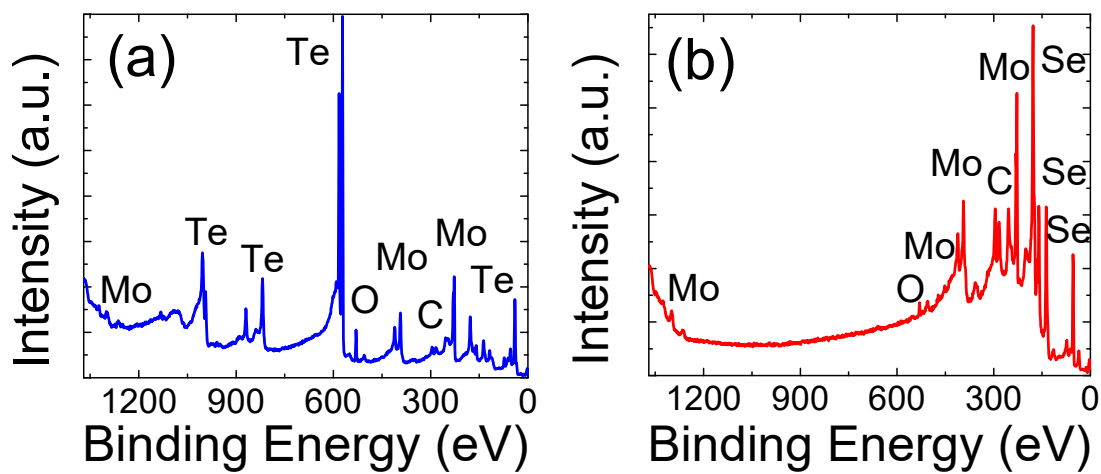


Figure S3 *In situ* XPS survey scans from (a) MoTe_2 and (b) MoSe_2 thin films.

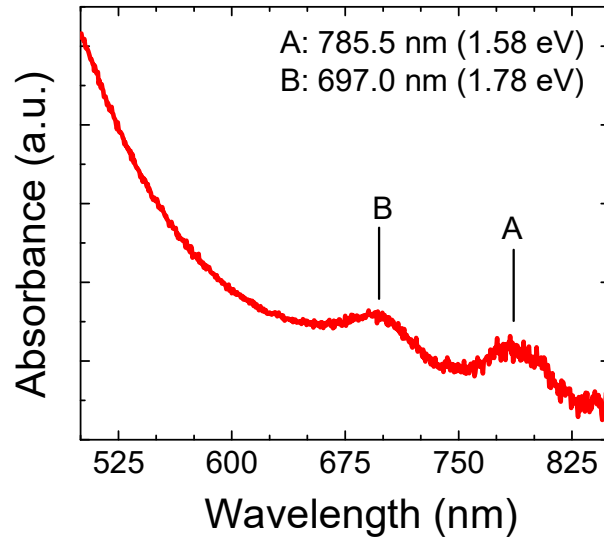


Figure S4 UV-Vis absorption spectra of a 5 nm MoSe₂ thin film at room temperature show the two characteristic exciton peaks, A and B.

S5: X-TEM of MoTe₂ and MoSe₂

Figure S5 shows the low-magnification X-TEM micrographs of the MoTe₂ and MoSe₂ thin films. The thickness of the films used for X-TEM was around 4-5 nm. The films seem to be continuous without any pinholes or discontinuities. The higher magnification X-TEM image in Figure S5(d) shows grain-like features, with grain sizes around 10-20 nm.

S6: Plan-view TEM of MoTe₂ and MoSe₂

Figure S6(a) shows the as-captured plan-view TEM image of MoTe₂ transferred onto a holey carbon grid. The grain structure is apparent. Due to high reactivity of MoTe₂ in ambient conditions, some of the defects are likely to be generated during the transfer process. Figure S6(b) shows the plan-view TEM image of MoSe₂ in a region with a wrinkle generated during the transfer process, thereby exposing the layered structure. An interlayer spacing of $\sim 6.7 \text{ \AA}$ is extracted.

S7: Arrhenius Fit to Electrical Data

Figure S7(a) and (b) show Arrhenius fits to the temperature dependent conductivity of MoTe₂ and MoSe₂, respectively. The extracted values of activation energy are abnormally low ($E_a \sim 18 \text{ meV}$ for MoTe₂, and $\sim 14 \text{ meV}$ for MoSe₂), and therefore we use a 2D VRH model.

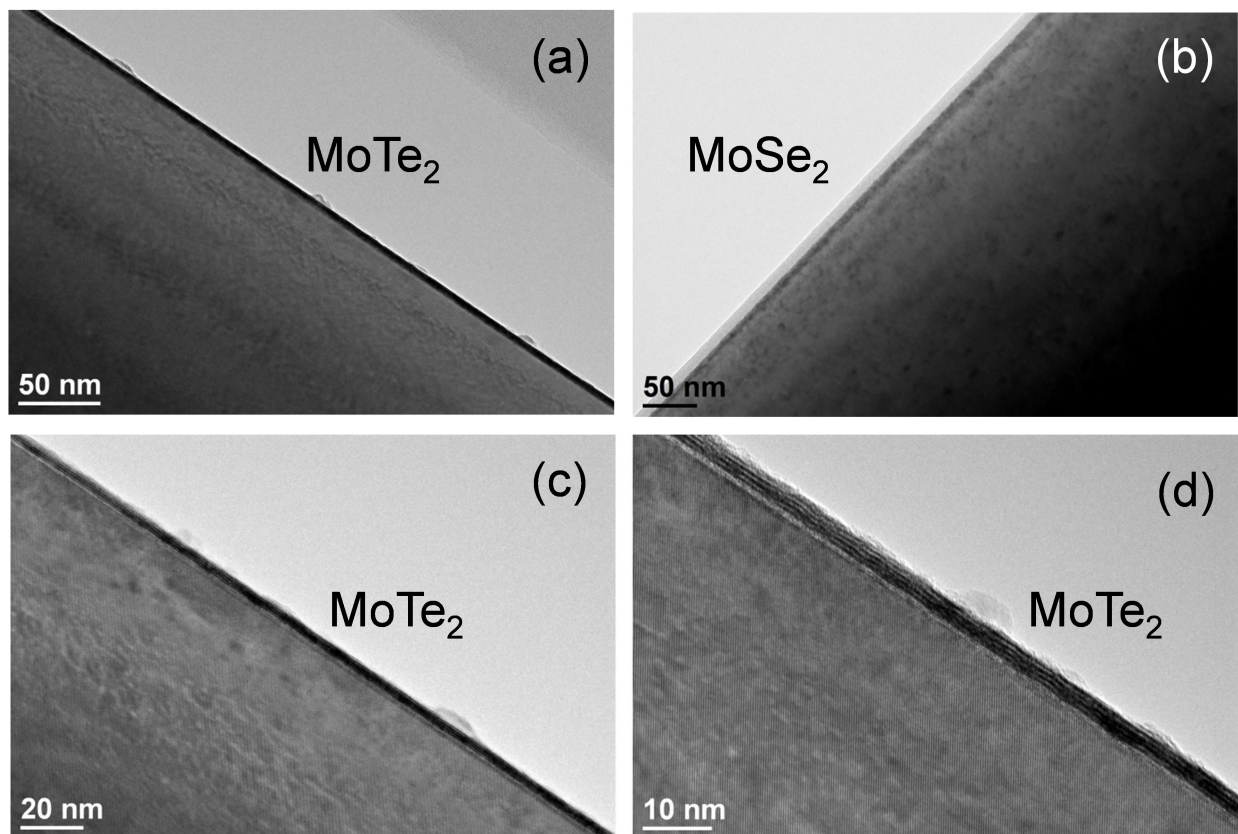


Figure S5 Low-magnification X-TEM micrographs of MoTe₂ and MoSe₂ show full film coverage on the substrate. (a) and (b) show large area MoTe₂ and MoSe₂ films over several hundred nm. (c) and (d) show MoTe₂ films at a higher magnification.

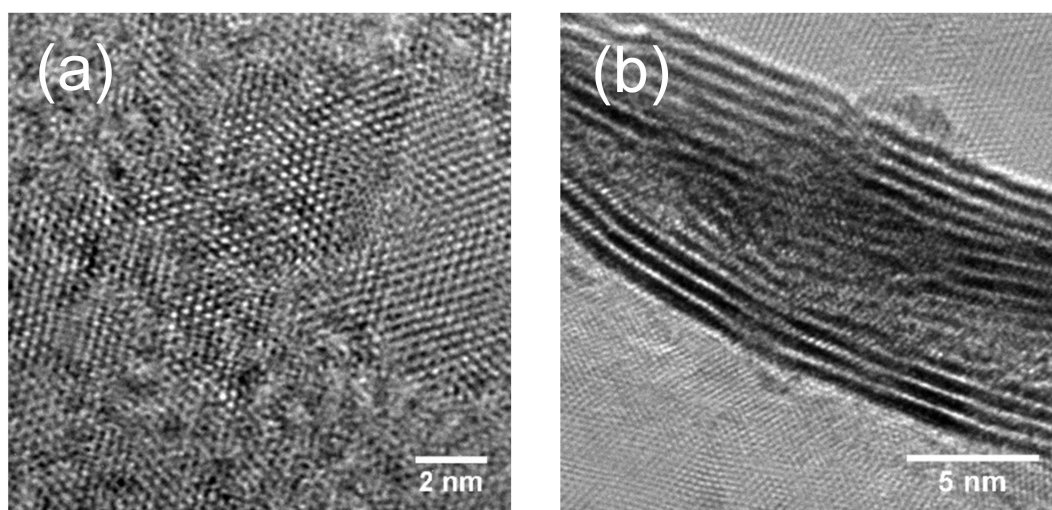


Figure S6 (a) Plan-view TEM micrograph of MoTe₂ shows its grainy structure. (b) Plan-view TEM micrograph of MoSe₂ in a wrinkled region uncovers its layer structure.

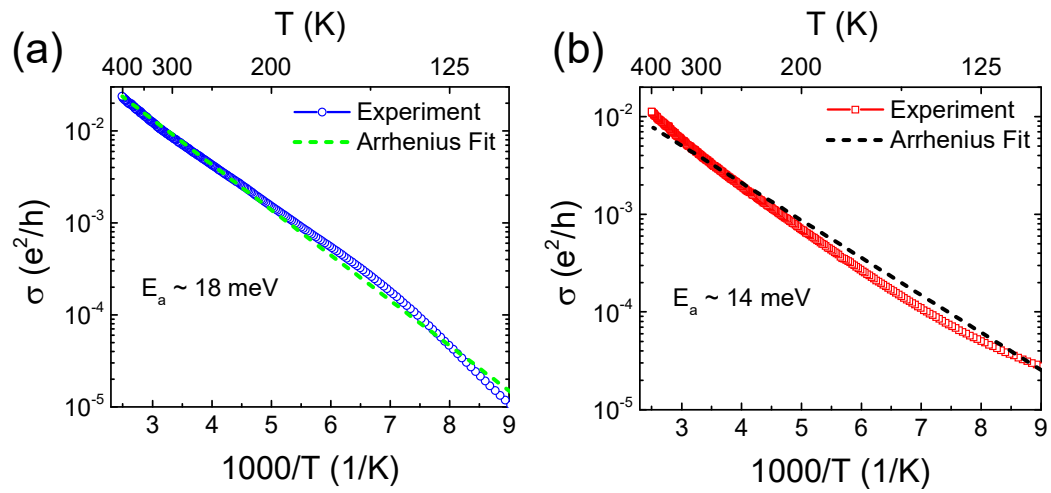


Figure S7 Arrhenius fits to the temperature dependent conductivity plotted on a semi-log scale for (a) MoTe₂ and (b) MoSe₂ result in abnormally low values of activation energy.

References

- (1) Zhang, Y.; Chang, T.-R.; Zhou, B.; Cui, Y.-T.; Yan, H.; Liu, Z.; Schmitt, F.; Lee, J.; Moore, R.; Chen, Y.; Lin, H.; Jeng, H.-T.; Mo, S.-K.; Hussain, Z.; Bansil, A.; Shen, Z.-X. Direct Observation of the Transition from Indirect to Direct Bandgap in Atomically Thin Epitaxial MoSe₂. *Nat Nano* **2014**, *9* (2), 111–115.
- (2) Wang, K.; Feng, Y.; Chang, C.; Zhan, J.; Wang, C.; Zhao, Q.; Coleman, J. N.; Zhang, L.; Blau, W. J.; Wang, J. Broadband Ultrafast Nonlinear Absorption and Nonlinear Refraction of Layered Molybdenum Dichalcogenide Semiconductors. *Nanoscale* **2014**, *6* (18), 10530–10535.